metals

MDPI

Article

The Challenges of Modeling Defect Behavior and Plasticity across Spatial and Temporal Scales: A Case Study of Metal Bilayer Impact

Leah Granger [1], Muh-Jang Chen [2], Donald Brenner [3,*] and Mohammed Zikry [2,*]

[1] Department of Chemical and Biomolecular Engineering, North Carolina State University, Raleigh, NC 27695, USA
[2] Department of Mechanical and Aerospace Engineering, North Carolina State University, Raleigh, NC 27695, USA
[3] Department of Materials Science and Engineering, North Carolina State University, Raleigh, NC 27695, USA
* Correspondence: brenner@ncsu.edu (D.B.); zikry@ncsu.edu (M.Z.)

Abstract: Atomistic molecular dynamics (MD) and a microstructural dislocation density-based crystalline plasticity (DCP) framework were used together across time scales varying from picoseconds to nanoseconds and length scales spanning from angstroms to micrometers to model a buried copper–nickel interface subjected to high strain rates. The nucleation and evolution of defects, such as dislocations and stacking faults, as well as large inelastic strain accumulations and wave-induced stress reflections were physically represented in both approaches. Both methods showed similar qualitative behavior, such as defects originating along the impactor edges, a dominance of Shockley partial dislocations, and non-continuous dislocation distributions across the buried interface. The favorable comparison between methods justifies assumptions used in both, to model phenomena, such as the nucleation and interactions of single defects and partials with reflected tensile waves, based on MD predictions, which are consistent with the evolution of perfect and partial dislocation densities as predicted by DCP. This substantiates how the nanoscale as modeled by MD is representative of microstructural behavior as modeled by DCP.

Keywords: molecular dynamics; dislocation density-based crystalline plasticity; dislocations; stacking faults; partial dislocation densities; spall

Citation: Granger, L.; Chen, M.-J.; Brenner, D.; Zikry, M. The Challenges of Modeling Defect Behavior and Plasticity across Spatial and Temporal Scales: A Case Study of Metal Bilayer Impact. *Metals* **2022**, *12*, 2036. https://doi.org/10.3390/met12122036

Academic Editor: Alain Pasturel

Received: 13 October 2022
Accepted: 23 November 2022
Published: 26 November 2022

1. Introduction

Large strain inelastic deformation and damage modes are inherently (and from a modeling viewpoint, frustratingly) multiscale processes. The nucleation of individual defects, such as dislocations and stacking faults, occurs through complex atomic-scale processes, the rate of which can depend on relatively long-range stress, strain, and defect distributions, which in turn are coupled to the microstructural mechanisms, such as grain-boundaries (GBs), texture, and grain morphology [1]. For example, collections of dislocations, once atomistically nucleated, propagate in a concerted motion that depends on the density, interactions with interfaces, surfaces, second phases, GBs, and a myriad of other interrelated microstructural elements. Atomic scale modeling approaches, such as molecular dynamics (MD), can provide important insights into complex nucleation and propagation processes, but they are inherently limited to relatively short time and length scales (typically sub-microsecond and sub-micron) depending on available computing resources and the accuracy of numerical algorithms [2]. Dislocation density-based crystalline plasticity (DCP) approaches are formulated to model the evolution of plasticity, once defect nucleation has occurred, as a function of slip rates and dislocation density evolution along preferred slip systems for large strain plasticity. One challenge, however, is to accurately describe

the complex atomic processes of defect nucleation at the atomic scale, such that defects, such as single dislocations, can evolve into total and partial dislocation densities or defect populations that are physically linked with nucleation events [3,4].

Because total and partial dislocation densities and slip rates are proportional to the Orowan velocities, they increase with increasing strain rates and impact velocities. When subjected to high-speed impacts, dislocation densities are also susceptible to viscous-drag effects attributed to strain rate sensitivity [5]. It further underscores that the rate sensitivity of crystalline materials can be affected by viscous effects and phonon drag [6]. Experimental observations of different dislocation microstructures that had been shocked using laser ablation ultrafast pulses/shock guns have been reported [7]. These experimental investigations provide insightful observations of the final state dislocation microstructure at specific times. However, what is missing from these experiments is the evolution mechanisms that track the nucleation of single perfect dislocations, such as edge and screw dislocations and single partial dislocations, such as Shockley and Hirth partials, to partial and total dislocation densities along specific slip directions and orientations.

This behavior can be further difficult to predict due to high strain rate failure modes, such as spalling. Spalling failure, which can occur under impact and high strain rate loads, occurs due to the tensile stress that exceeds the spalling strength. These tensile stresses are due to complex stress wave interactions of incident, reflection, and transmission waves [7–11]. Tensile stresses, pertaining to dislocation density activities, cause large inelastic deformation modes, which can lead to void nucleation and coalescence [8–11]. Stress accumulations near void perimeters exacerbate spalling failure and may, with enough impact momentum, eventually lead to opening mode stresses and failure as the spalling strength is exceeded. These high strain rate deformation modes are therefore well suited for MD [12,13] and DCP dynamic analyses, such as plate impact, to investigate a multiscale high strain rate problem to study defect nucleation and the evolving large strain plasticity modes.

The goal of this paper is to compare how MD and DCP can be used together to fundamentally understand and predict the nucleation of single dislocation and partial dislocations that evolve to total and partial dislocation densities, such that large strain inelastic modes are tracked from picoseconds to nanoseconds and across length scales from angstroms to nanometers. We identify how tensile stresses can occur due to high compressive strain rates, and how this can be, in combination with dislocation density evolution and accumulation, a precursor to spall. We do not attempt to describe the same scales and conditions for the two methods, but rather our intent is to detail how these methods approach a similar high strain rate example problem, what analyses and insights can come from these approaches, and how these insights are delineated based on relevant temporal and spatial scales. More critically, we do not attempt to force arbitrary linkages to both methods, such that predictions and physical understanding are numerically correlated to be consistent. To this end, we have chosen as an example an impact into a metal surface with a buried interface. This system is sufficiently complex to illustrate the different types of inelastic large strain modes and defects, including nucleation at the atomic scale and propagation at the micron scale of different types of dislocations, and the interaction of these dislocations to total and partial dislocation densities within a physically representative microstructure.

2. Computational Methods

In this section, brief descriptions are given for the MD and DCP models. More details can be found in [2,14,15].

2.1. Molecular Dynamics

Fundamentally, MD is a straightforward technique. Atoms are treated as classical particles, with their motion simulated by numerically integrating a set of classical equations of motion that are coupled through the interatomic interactions. Constraints can be added

to either the classical equations of motion or through the method by which they are solved to simulate different thermodynamic ensembles for equilibrium systems [14]. MD can also simulate non-equilibrium systems, including chemical dynamics, where the atomic dynamics are complex [16,17].

The challenge and power of MD comes with the use of many body forces that are intended to model the interactions that occur between atoms. These interactions can be obtained from electronic structure calculations, from interatomic potentials that attempt to replace explicit electrons with effective interactions, or from machine learning potentials that train generalized functions to reproduce forces from atoms generated from other approaches (e.g., Density Functional Theory) [18,19]. The quantitative accuracy of MD simulations (subject to the constraints of treating atoms as classical objects) is often tied to how well the atomic interactions describe the true system, but new insights can also come from very approximate potentials [20,21].

Because defects originate at the atomic scale, MD provides the detail needed to observe dislocation nucleation. Potentials best suited for modeling mechanical behavior and defect energies are often those based on the principles of quantum mechanical bonding [18,19]. One such example commonly used in modeling metals is the embedded atom method (EAM) [22]. This approach treats multibody interactions through the effects of each atom's local electron environment (the embedding energy) in addition to pair interactions. The computational efficiency of EAM allows calculations on a scale sufficiently large to observe extended defects and dislocations in metallic systems.

System setup and the method to initiate defects vary according to the crystalline and microstructural structure. Early shock simulations [23,24] used scaling of a periodic box size in one direction, or a piston or flyer plate with periodic boundaries in directions transverse to the shockwave. Alternatively, shockwaves may be induced by a non-periodic impactor or projectile, but in this case a large target is necessary to minimize edge effects [25–27].

2.2. Dislocation Density-Based Crystalline Plasticity (DCP) Simulations

The dislocation density-based crystalline plasticity formulation accounts for large strain deformation and the evolution of immobile and mobile dislocation densities. Details of this approach are given in [15], and it is only briefly outlined here.

The dislocation density-based formulations assume that the total dislocation densities of each slip system can be decomposed into mobile and immobile parts as

$$\frac{d{\rho_m}^{\alpha}}{dt} = \left|\dot{\gamma}^{\alpha}\right|\left(\frac{{g^{\alpha}}_{sour}}{b^2} - {g^{\alpha}}_{mnter-}{\rho^{\alpha}}_{m} - \frac{{g^{\alpha}}_{immob-}}{b}\sqrt{{\rho^{\alpha}}_{im}}\right), \tag{1}$$

$$\frac{d{\rho_{im}}^{\alpha}}{dt} = \left|\dot{\gamma}^{\alpha}\right|\left({g^{\alpha}}_{mnter+}{\rho^{\alpha}}_{m} + \frac{{g^{\alpha}}_{immob+}}{b}\sqrt{{\rho^{\alpha}}_{im}} - {g^{\alpha}}_{recov}{\rho^{\alpha}}_{im}\right), \tag{2}$$

where the superscript α represents the FCC slip systems given in Table 1; g_{sour} corresponds to the source term mobile dislocation densities, g_{mnter} stands for obstacles, such as immobile dislocations and forest dislocations, trapping mobile dislocations; g_{immob} corresponds to the immobilization of the mobile dislocations; g_{recov} represents the annihilation n of immobile dislocation densities. The expressions of these coefficients are shown in Table 2, where l_c is the length of junctions; b is the magnitude of Burgers vectors; f_o is an interaction fraction constant; $\dot{\gamma}^{\alpha}$ is the slip rate. As seen from (1) and (2), the evolution equations couple the immobile and mobile dislocation densities with the slip rate and the dislocation density interactions. These values are treated as unknowns and updated at each solution increment in the nonlinear computational framework.

Table 1. FCC slip system designation.

α,β=	1	2	3	4	5	6	7	8	9	10	11	12
Plane	(111)	(111)	(111)	$(\bar{1}11)$	$(\bar{1}11)$	$(\bar{1}11)$	$(\bar{1}\bar{1}1)$	$(\bar{1}\bar{1}1)$	$(\bar{1}\bar{1}1)$	$(1\bar{1}1)$	$(1\bar{1}1)$	$(1\bar{1}1)$
Direction	$[\bar{1}01]$	$[\bar{1}\bar{1}0]$	$[0\bar{1}\bar{1}]$	[011]	$[\bar{1}\bar{1}0]$	[101]	[101]	[110]	$[0\bar{1}\bar{1}]$	[011]	[110]	$[\bar{1}01]$

Table 2. Coefficients for the evolution equations.

g	**Expression**
g^{α}_{sour}	$b^{\alpha}\varphi\sum_{\beta}\sqrt{\rho^{\beta}_{im}}$
g^{α}_{mnter-}	$l_c f_o \sum_{\beta}\sqrt{a_{\alpha\beta}}\left(\frac{\rho^{\beta}_{m}}{\rho^{\alpha}_{m}b^{\alpha}}+\frac{\dot{\gamma}^{\beta}_{m}}{\dot{\gamma}^{\alpha}_{m}b^{\beta}}\right)$
g^{α}_{immob-}	$\frac{l_c f_o}{\sqrt{\rho^{\alpha}_{im}}}\sum_{\beta}\sqrt{a_{\alpha\beta}}\rho^{\beta}_{im}$
g^{α}_{mnter+}	$\frac{l_c f_o}{\dot{\gamma}^{\alpha}\rho^{\alpha}_{m}}\sum_{\beta,\gamma} n^{\beta\gamma}_{\alpha}\sqrt{a_{\beta\gamma}}\left(\frac{\rho^{\gamma}_{m}\dot{\gamma}^{\beta}}{b^{\beta}}+\frac{\rho^{\beta}_{m}\dot{\gamma}^{\gamma}}{b^{\gamma}}\right)$
g^{α}_{immob+}	$\frac{l_c f_o}{\dot{\gamma}^{\alpha}\sqrt{\rho^{\alpha}_{im}}}\sum_{\beta} n^{\beta\gamma}_{\alpha}\sqrt{a_{\beta\gamma}}\rho^{\gamma}_{im}\dot{\gamma}^{\beta}$
g^{α}_{recov}	$\frac{l_c f_o}{\dot{\gamma}^{\alpha}\sqrt{\rho^{\alpha}_{im}}}\left(\sum_{\beta}\sqrt{a_{\beta\gamma}}\frac{\dot{\gamma}^{\beta}}{b^{\beta}}\right)\exp\left(\frac{-H_0+H_0\sqrt{\rho^{\alpha}_{im}/\rho_s}}{kT}\right)$

The reference shear stresses, τ_{ref}, which accounts for the hardening behavior for each slip system is

$$\tau^{\alpha}{}_{ref} = \tau_y + G\sum_{\beta=1}^{nss} b^{(\beta)}\sqrt{a_{\alpha\beta}\rho^{\beta}{}_{im}}, \tag{3}$$

where *nss* is the number of the slip system, G is the shear modulus, and $\tau_y{}^{\alpha}$ is the static shear yield stress of slip system α.

Based on different dynamic experiments [28,29], partial dislocation densities and perfect dislocation densities have been observed to play a dominant role in the high strain rate mechanical behavior of crystalline systems. Perfect dislocation densities can decompose into Shockley partial dislocation densities and form Lomer and Hirth partials. To account for the decomposition of perfect dislocation densities into partials, a minimal energy criterion is used to identify resultant partials for each perfect dislocation density interaction [15,28–30]. We can, then, assume that the perfect dislocation densities relevant to each interaction can be obtained by a distribution tensor, $\varrho_{\alpha\beta} \in R^{12\times 12}$ as

$$\varrho_{\alpha\beta} = \frac{\rho^{\alpha}{}_{im} \otimes \rho^{\beta}{}_{im}}{\sum_{i=1}^{12}\rho^{i}{}_{im}}, \tag{4}$$

where α and β correspond to the different slip systems. A mapping tensor, $J_{\alpha\beta p} \in R^{12\times 12\times 21}$, is then used to determine the density of the partial dislocation density, ρ_p, by using the tensor product with the distribution tensor (Equation (5)). This mapping tensor is formed by Boolean numbers that contain the active partial dislocation densities for each interaction. The space is mapped from the 12 by 12 slip system combinations to the 21 possible partial dislocation densities. These 21 partials are 12 Shockley, 6 Lomer, and 3 Hirth partial dislocation densities, and are given by

$$\rho_p = \varrho_{\alpha\beta} J_{\alpha\beta p}. \tag{5}$$

A summary of these partial dislocation densities is given in Table 3.

Table 3. Partial dislocation densities ρ_p.

Shockley	ρ_1	$\frac{1}{6}[\bar{1}\bar{1}2]$	Shockley	ρ_8	$\frac{1}{6}[\bar{1}1\bar{2}]$	Lomer	ρ_{15}	$\frac{1}{3}[101]$
	ρ_2	$\frac{1}{6}[\bar{1}2\bar{1}]$		ρ_9	$\frac{1}{6}[\bar{1}\bar{2}1]$		ρ_{16}	$\frac{1}{3}[\bar{1}01]$
	ρ_3	$\frac{1}{6}[2\bar{1}\bar{1}]$		ρ_{10}	$\frac{1}{6}[121]$		ρ_{17}	$\frac{1}{3}[01\bar{1}]$
	ρ_4	$\frac{1}{6}[112]$		ρ_{11}	$\frac{1}{6}[1\bar{1}\bar{2}]$		ρ_{18}	$\frac{1}{3}[1\bar{1}0]$
	ρ_5	$\frac{1}{6}[\bar{2}1\bar{1}]$		ρ_{12}	$\frac{1}{6}[\bar{2}\bar{1}1]$	Hirth	ρ_{19}	$\frac{1}{3}[001]$
	ρ_6	$\frac{1}{6}[1\bar{2}\bar{1}]$	Lomer	ρ_{13}	$\frac{1}{3}[110]$		ρ_{20}	$\frac{1}{3}[100]$
	ρ_7	$\frac{1}{6}[211]$		ρ_{14}	$\frac{1}{3}[011]$		ρ_{21}	$\frac{1}{3}[010]$

3. Results

The impact of a buried metal–metal interface was modeled by both MD and DCP, with the goal of describing how defect evolution is coupled to the material's interface and impact conditions. The setup for the simulations is summarized in Table 4. Both use a finite size impactor with a specified initial velocity that impacts a substrate comprised of a relatively thin film of copper on nickel. For the MD model, the impacted surface was 38.68 nm × 38.68 nm, with depth in the impact direction of 19.40 nm. For the DCP plane strain finite element mesh, the substrate was 193 µm wide and 194 µm deep in the impact direction. A nonlinear FE research code developed by Zikry for crystalline plasticity was used [cf. 15]. The system had a dimension of 1 m in the thickness direction.

Table 4 shows the copper film thickness, the impactor width, and the maximum depth to which the impactor penetrates the substrate for the simulations. The aspect ratio between the impactor diameter and film thickness (ID/FT) are comparable between the MD and DCP models. However, the dynamics of the flyer differ between the two methods. For the MD model, the impactor slows as the plate transfers its kinetic energy to the substrate, while the DCP impactor has a constant compression speed and abruptly stops when it reaches 2.5% nominal stain (14.74 ns). Two initial velocities were used for the MD. The lower initial velocity of 500 m/s results in a similar percentage of penetration into the copper film as the DCP simulations. However, as explained below, the two methods yield different results regarding subsurface defects at the buried interface, and, therefore, a second MD simulation was carried out with a larger plate velocity and hence larger penetration depth.

Table 4. Comparison of system setups.

Method	Cu Film Thickness (FT)	Impactor Diameter (ID)	Initial Impact Velocity	Maximum Penetration Depth (PD)	ID/FT	PD/FT
MD	4 nm	3.8 nm	500 m/s	0.36 nm	95%	9%
MD	4 nm	3.8 nm	1500 m/s	2.2 nm	95%	55%
DCP	43 µm	64 µm	340 m/s	5.0 µm	149%	12%

DCP and MD inherently describe material properties differently. The DCP simulation assumes isotropic properties for the elastic regime, while accounting for large strain plasticity based on the DCP formulation. It also includes as inputs Young's modulus and Poisson's ratio. MD, on the other hand, makes no assumptions about material properties being isotropic, but instead fits an interatomic potential, such as the EAM, to a set of properties. For example, these may include lattice constants, cohesive energy, linear elastic constants, and defect energies. Table 5 shows a comparison of some of the mechanical properties for copper and nickel used in the DCP and those from the EAM potential used in the MD. The shear modulus, Poisson's ratio, and Young's modulus reported for MD were calculated according to the Voigt–Reuss–Hill theory [31] using the elastic constants from the EAM potential.

Table 5. Comparison of material properties.

	Copper		Nickel	
	EAM	**DCP**	**EAM**	**DCP**
a_0 (nm)	0.3615	0.3615	0.352	0.352
Young's Modulus, *E* (GPa)	119.2	110	204.0	200
Bulk Modulus, *B* (GPa)	138.4	91.7	181.0	167
C_{11} (GPa)	169.9	148	241.3	269
C_{12} (GPa)	122.6	63.5	150.8	115
C_{44} (GPa)	76.2	42.3	127.3	76.9
Shear Modulus (GPa)	43.92	42.3	77.72	76.9
Poisson's Ratio, ν	0.36	0.3	0.31	0.3
Static Yield Stress (MPa)	-	110	-	110
Initial Mobile Density (m^{-2})	-	10^6	-	10^6
Initial Immobile Density (m^{-2})	-	10^8	-	10^8
Saturation Density (m^{-2})	-	10^{14}	-	10^{14}

Molecular Dynamics Simulations

A copper/nickel bilayer was used as a model system since MD potentials were readily available and the high symmetry of their face centered cubic (FCC) structure aids analysis; a cylindrical projectile was used to allow investigation of deformation due to compression directly below impact as well as propagation outward into the bulk material. Each layer is oriented such that the free surfaces and the interface are the (001) plane (Figure 1). The lateral dimensions were selected such that the edge mismatch between layers was minimized. Periodic boundaries were used in the x and y directions, and atomic stress was used to monitor the progression of the resulting compression wave through the target to ensure the relevant timeframe does not include wrap-around effects of the periodic boundaries or reflection from the lower surface. The timestep was chosen as 0.2 femtoseconds.

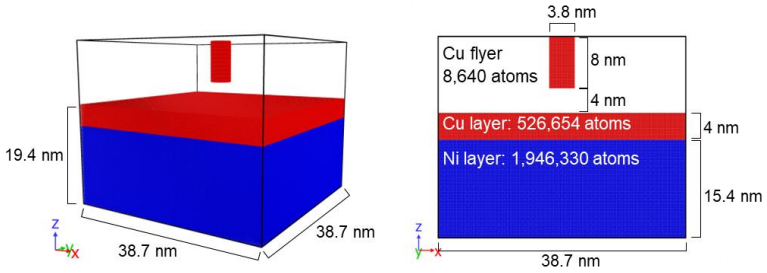

Figure 1. The perspective and front views of the Cu/Ni bilayer and cylindrical Cu flyer plate where Cu atoms are shown in red and Ni in blue.

We used the LAMMPS code [32] and the EAM potentials for copper and nickel [33]. The system energy was first minimized, followed by equilibration of the bilayer using a Langevin thermostat set to 300 K for 20 ps followed by an additional 20 ps of equilibration without a thermostat applied. The flyer plate, treated as a rigid body, was given an initial velocity of either 0.5 km/s or 1.5 km/s downwards in the [001] direction. The local structure was characterized using the Ackland algorithm [34], and the stress per atom tensor [35] was calculated during the simulation. Dislocation analysis was conducted using a common neighbor analysis (CNA) [36,37] and the dislocation extraction algorithm (DXA) [38], as implemented in OVITO [39]. OVITO was also used for visualization and all non-graphical images.

The lattice mismatch between copper and nickel resulted in dislocations being created at the interface during the energy minimization. For this orientation, the mismatch leads to perfect dislocations on a grid pattern along the interface as illustrated by the line dislocations colored blue, most easily seen in the top views shown in Figure 2.

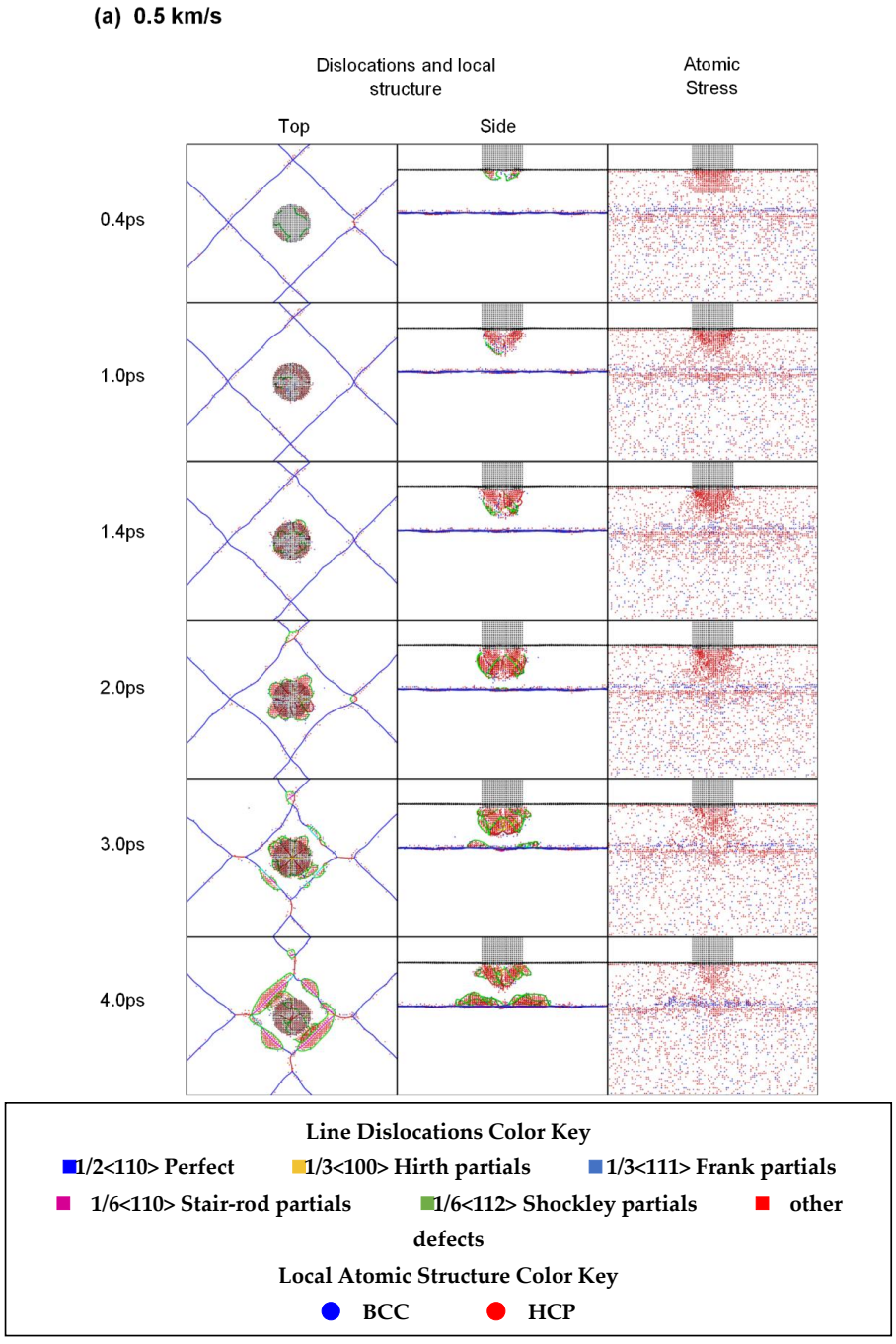

Figure 2. *Cont.*

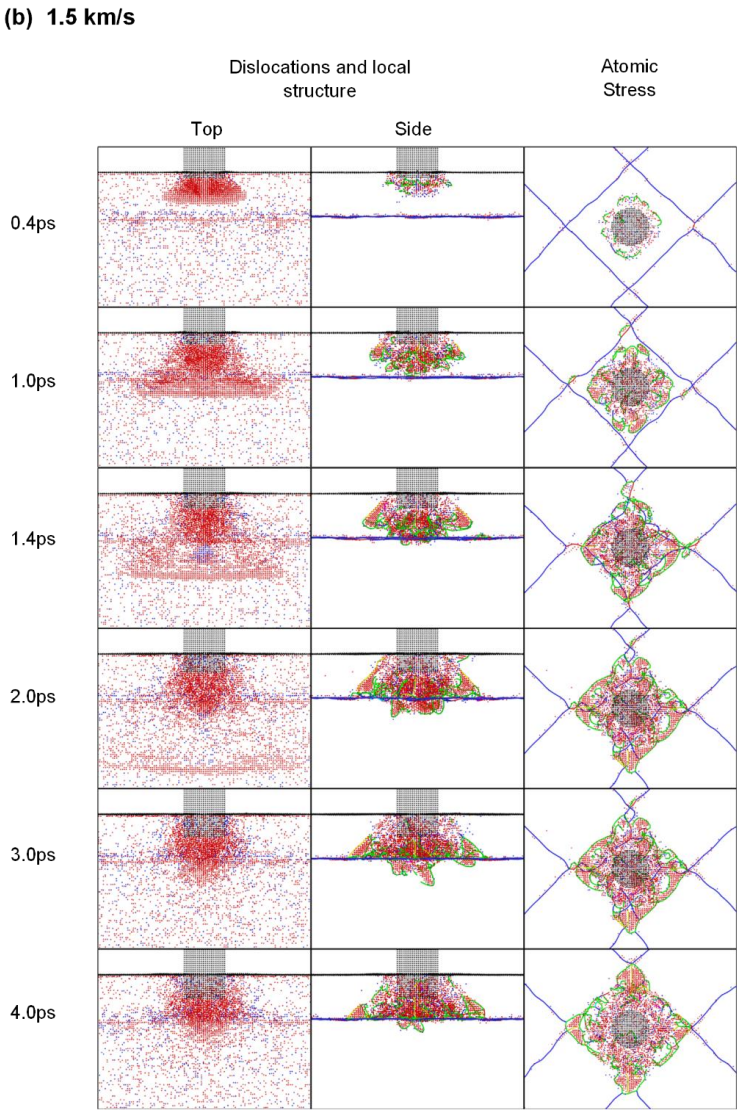

Figure 2. Simulation snapshots illustrating the local structure and line dislocations for the top and side views and the atomic stress for the side view for an initial impactor velocity of (**a**) 0.5 km/s and (**b**) 1.5 km/s. Note that images are zoomed in to the region of interest and do not show the entire system Atoms of the impactor and top surface are shown in black. Dislocation and local structure visualization includes both line dislocations (shown as smooth lines colored according to the key) and bulk atoms with a local structure other than FCC or uncategorized (shown as points colored according to the key). For stress visualization, only atoms with atomic stress normal to the plane of impact such that $|S_z| > 1.3 \times 10^{-19}$ Pa·m^3 are visualized.

For the impactor with an initial velocity of 0.5 km/s, a weak compression wave is created ahead of the impactor that largely dissipates when it reaches the buried interface. This is illustrated in Figure 2 by the atomic stress in the z direction, where a weak wave front (compared to the higher impact energy, see below) is barely visible. Impact-induced Shockley dislocations, as determined by DXA and visible at the impactor–substrate contact, are first observed at approximately 0.3 ps following impact at the perimeter of the impactor. These propagate along (111) planes primarily in the directions leading under the impactor. As the simulation progresses, and the defects below the impactor approach the copper–nickel interface, the interfacial dislocations formed during energy minimization expand into the copper as separate stair-rod and Shockley partial dislocations. The two dislocation regions (the one below the impactor and the one at the interface) do not meet, and no dislocations appear in the nickel.

Increasing the impactor's velocity to 1.5 km/s provides sufficient energy to initiate a well-defined compression wave, illustrated by planes of atoms of high atomic stress that pass through the copper–nickel interface. Dislocations again initially form along the perimeter of the impactor, but in this case, they propagate both under and laterally from the impactor edge. Immediately before the defects under the impactor reach the nickel, illustrated in the 1.4 ps snapshot of Figure 2b, a region of atoms with positive atomic stress (indicating tension) is present under the flyer plate. This is similar to what is observed in the DCP model, but at a smaller scale (see below for details). Shockley dislocations then form in the nickel directly below the impactor, while the lateral dislocations in the copper are largely pinned at the interface. This results in a much smaller number of dislocations in the nickel compared to the copper. As the system continues to progress, the fraction of Hirth and stair-rod partial dislocations increases, as apparent from Figure 3b.

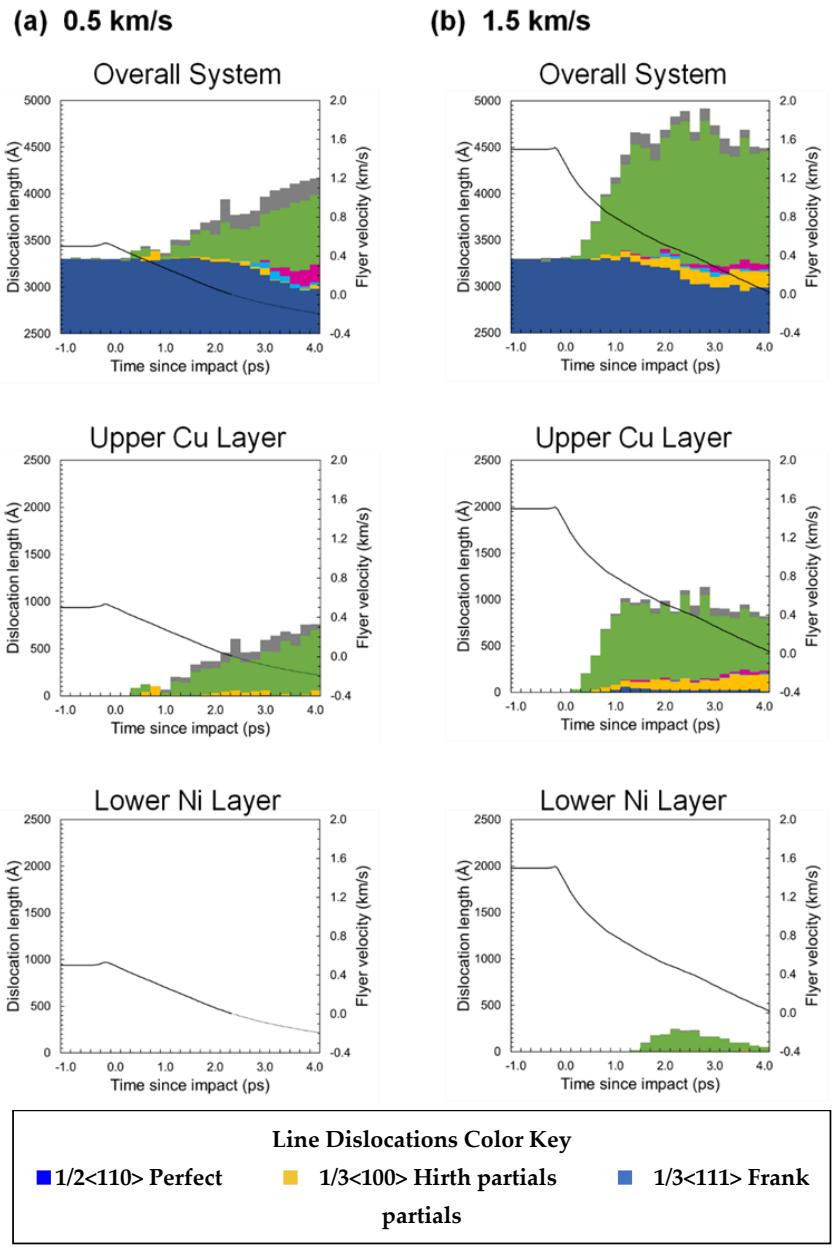

Figure 3. The relative lengths and types of line dislocations for initial impactor of (**a**) 0.5 km/s and (**b**) 1.5 km/s, plotted for the overall system (both layers including the interface) as well as for individual layers to show effect of interfacial interactions. The velocity of the impactor is also plotted such that the line is solid when the plate is moving downwards and dashed when moving upwards.

As an alternative way to quantify and visualize dislocation behavior in the system, the positions of any atoms with a non-FCC local structure were converted to radial coordinates and then plotted (Figure 4) to visualize position and local defect density, where defect refers to atoms not adhering to the bulk FCC structure. The defect density was calculated by normalizing the number of defect atoms by the volume of annular cylindrical bins of width 0.5 nm and height 0.5 nm. As shown in Figure 4, the defect density consistently agrees with phenomena observed in the previously discussed DXA analysis. For example, in the low-velocity case, the upward propagating defects present starting at 3 ps originate from interfacial mismatch defects. In the high-velocity case, particularly in the 2 ps frame, defects directly below the flyer plate can pass through to the lower layer, but the defects outside the plate diameter tend to slip along the surface instead. Although the same information is portrayed as above, this visualization provides a better comparison to that used in the following section.

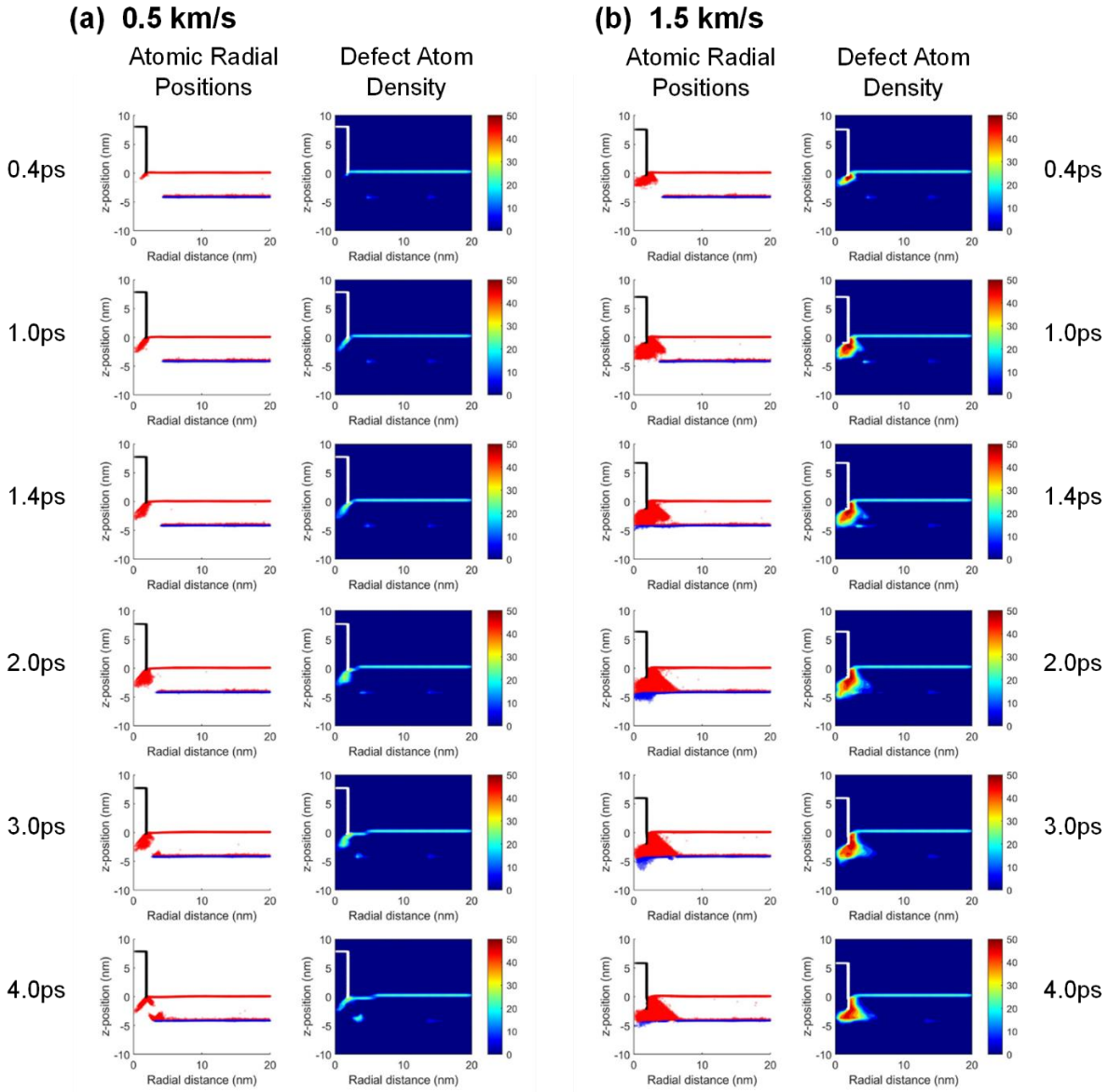

Figure 4. Radial coordinates visualization for MD simulations for initial impactor velocities of (**a**) 0.5 km/s and (**b**) 1.5 km/s. Only atoms with a non-FCC local structure are visualized, where Cu atoms are red, Ni atoms blue, and Cu atoms of the flyer in black (note: only surface atoms of the FCC impactor are non-FCC for visualization). Density contour plots are based on annular cylindrical bins with a width 0.5 nm and a height of 0.5 nm, and the impactor atomic positions are also visualized in white for reference.

4. High Strain-Rate Dislocation Density-Based Crystalline Plasticity

In parallel with the MD simulations, a plane strain finite element (FE) model (Figure 5a) for a bilayer composed of copper and nickel layers with the same cubic textures as MD was subjected to a high strain rate displacement load. The load resulted in a flyer velocity similar to but lower than the impact velocities used in the MD models. The material properties are given in Table 5, and the dimensions are given in Figure 5. The applied velocity of the flyer was 340 m/s for a nominal strain rate of 1.75×10^6 s^{-1}. There are 9506 elements and 10,000 timestep steps for a total time of 40 ns. The dynamic loading curve is plotted in Figure 5b. The dynamic FE scheme is based on an implicit trapezoidal rule and one-point integration with hourglass control [40]. An implicit time step scheme was used for stability, and the incremental timestep of 4 ps was chosen to be small enough to track wave propagation and for stable and accurate time integration.

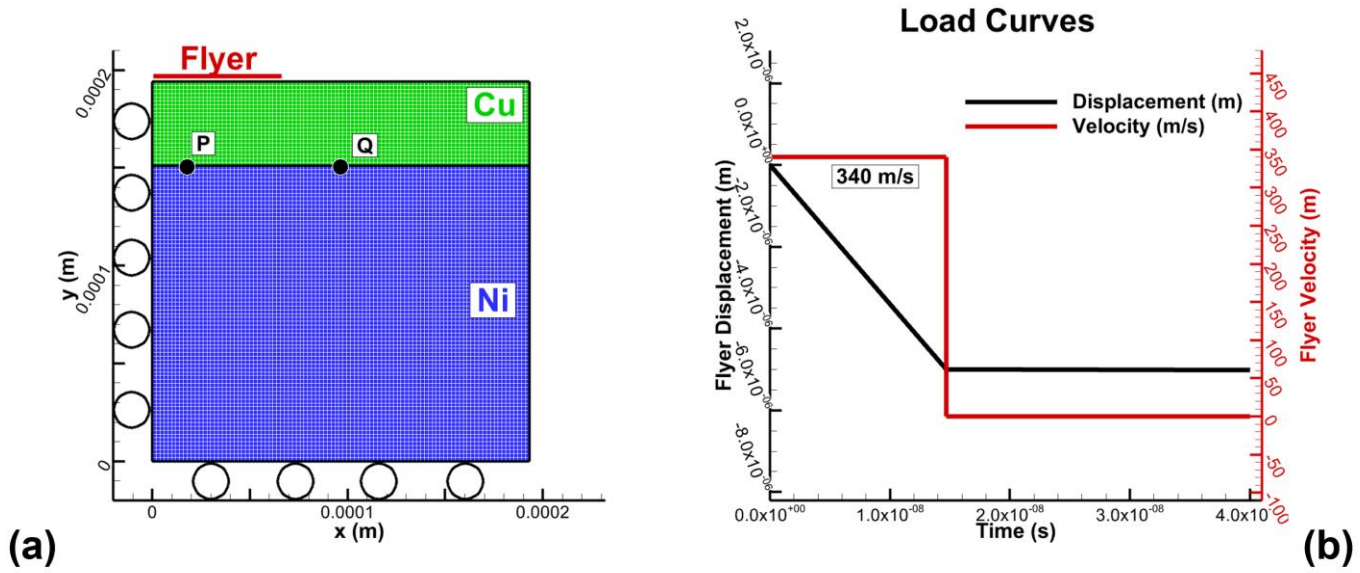

Figure 5. (**a**) Representation of the FE mesh that is subjected to the displacement load curves illustrated in (**b**) with a constant speed of 340 m/s for 14.73 ns.

The nominal stress as a function of time is plotted in Figure 6a. The stresses are normalized by the static yield stress and attain a maximum normalized value of approximately 100 (Figure 6a). To understand how stresses propagate from the flyer to the interface, normal stresses under the flyer (point P, Figure 5a) are compared with the normal stress along the interface (middle point Q), as seen in Figure 6b. The normal stress propagation shows a similar phenomenon on the two representative points, and the stresses are compressive at the interface at 14 ns. At 28 ns, there is a transition to tensile stresses for both points. The normal stress transition from compression to tension is similar to the spalling phenomenon that a tensile stress induces due to the reflections from the bottom and lateral sides [9,10]. Furthermore, the normal stress is higher under the flyer at Point P than at point Q. The maximum normalized compressive value at Point P is 109 and that of Point Q is 28.

To further understand the high strain rate effects of the propagating and evolving normal stresses, contours at two separate times, 14 nanoseconds (Figure 7a) and 28 nanoseconds (Figure 7b) are shown. As seen in Figure 7a, the normal stress attains a maximum normalized value of 160 at 14 ns near the interface. At 28 ns, after compressive waves have propagated through the interface into the nickel layer, the maximum normalized compressive stress is 93 (Figure 7b) in the nickel, and the maximum normalized tensile stress is 24 near the interface. This transition from compression to tension is crucial since it can indicate the onset of spalling due to the reflection of the compressive stresses to tensile stresses. This can also be related to increases in the immobile dislocation densities [10,41]. For the copper layer (Figure 7c) before 14 ns, the dominant slip systems, which are [101]$(\overline{1}11)$

and [$\bar{1}01$]($1\bar{1}\bar{1}$), have a normalized value of 89,000 (the immobile dislocation densities are normalized by the initial immobile dislocation density). As the stresses transition to tensile, slip systems [$\bar{1}01$](111), and [101]($1\bar{1}\bar{1}$) dominate (green) at approximately 28 ns. At 40 ns, the dislocation densities continue to increase in the copper to a normalized value 196,000 (Figure 7c), and the immobile densities' rate of increase essentially plateaus. For the nickel layer (Figure 7d), the immobile dislocation densities continue to increase, but the values are less than the copper layer, and the most active slip systems are different. At 40 ns, the dominant slip systems are [101]($\bar{1}1\bar{1}$) and [$\bar{1}01$]($1\bar{1}\bar{1}$), and the maximum normalized value is approximately 41,000, which is significantly lower than the maximum dislocation densities in the copper layer.

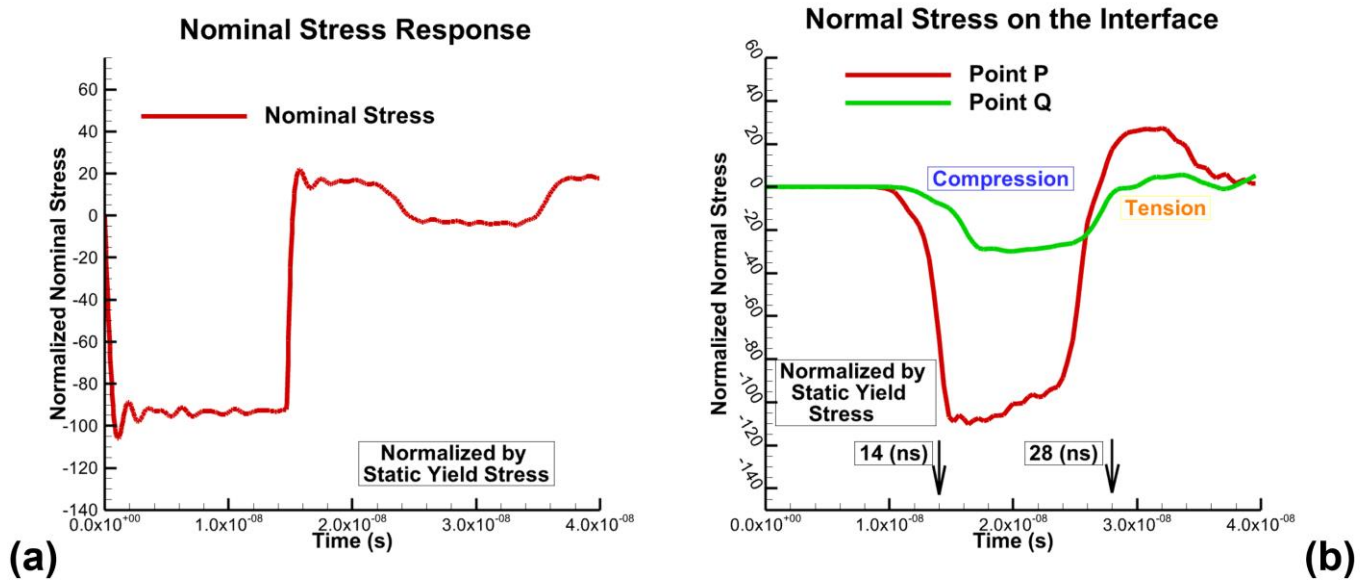

Figure 6. (**a**) Global nominal stress responses, (**b**) normalized normal stress, σ_{yy}; compressive stresses are at the interface at approximately 14 ns and tensile stress reaches the interface at around 28 ns.

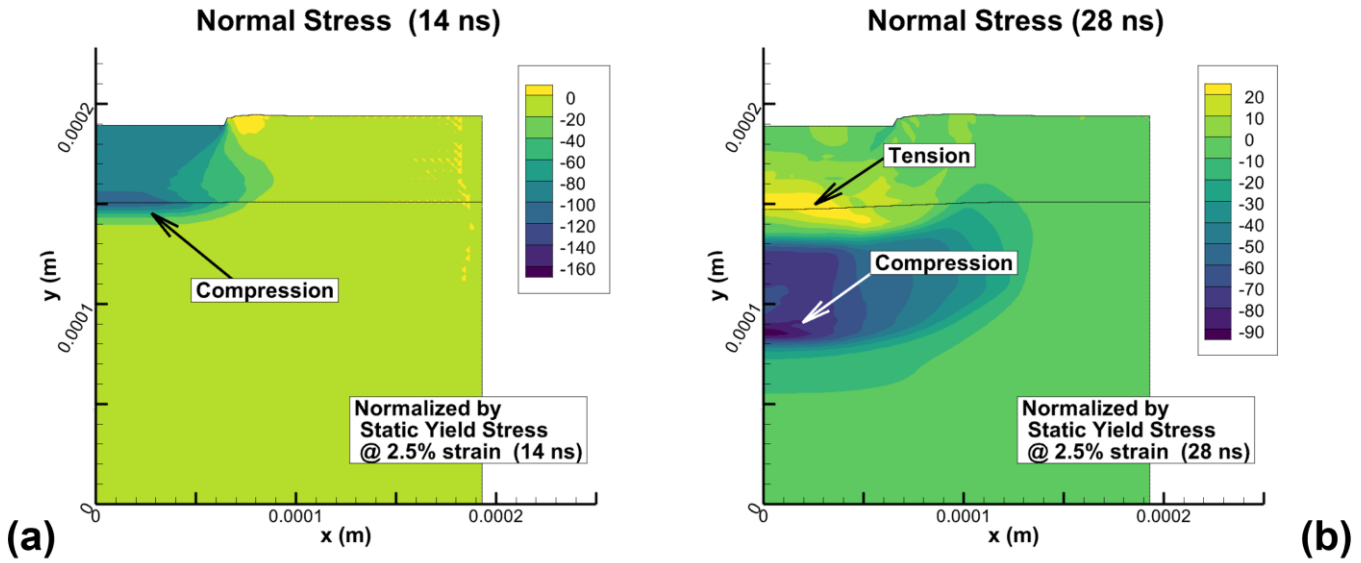

Figure 7. *Cont.*

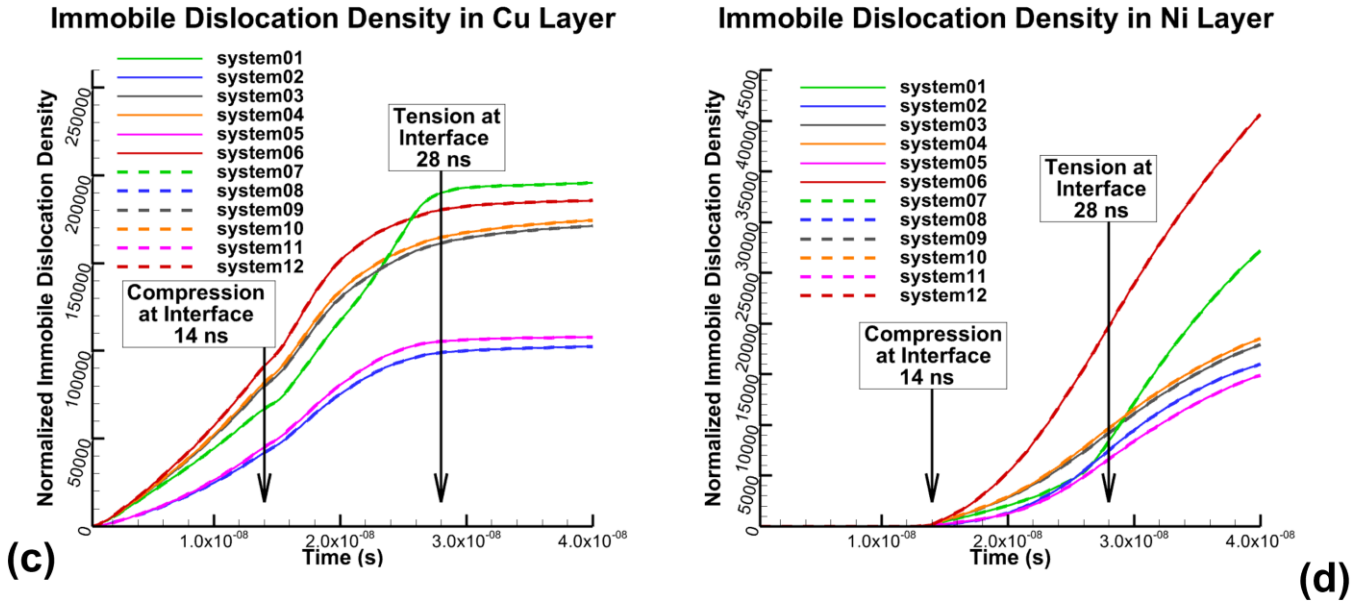

Figure 7. (**a**) Normal stress at a nominal strain of 2.5% at 14 nanoseconds, and (**b**) 28 nanoseconds. (**c**) normalized immobile dislocation densities in the copper layer, and (**d**) the nickel layer. At 14 nanoseconds, normal stresses are mostly compressive at the interface, at 28 nanoseconds normal stresses transition to tensile at the interface. The slip systems are given in Table 1.

The transition from compressive to tensile stresses also has a significant effect on the evolution of partial dislocation densities. The partial dislocation densities for each type are summarized, showing elements for both layers: the copper layer (Figure 8a) and the nickel layer (Figure 8b). The Shockley partials are more prevalent than Lomer–Cottrell and Hirth partials as indicated by the values of the immobile partial densities. The total densities of Shockley partial are generally three- to five-times higher than the Lomer–Cottrell and Hirth partials in the copper and nickel layers during the total elapsed time (Figure 8a,b). As previously shown, tensile behavior occurs at approximately 14 ns in the copper layer and at 28 ns in the nickel. The partial dislocation densities attain a plateau after the transition into the copper layer. However, in the thicker nickel layer, the partial dislocation densities increase at a faster rate than in the thinner copper layer. The contours at 40 ns of the most significant Shockley, $\frac{1}{6}[\overline{2}11]$, and Hirth partial, $^{1}/_{3}[100]$, dislocation densities show this partial dislocation density distribution (Figure 8c,d) at a nominal strain of 2.5%. The dislocation densities extend from the impact surface to the buried interface, which results in a discontinuity between two layers. The copper layer, especially around the flyer edge, has the higher dislocation densities with a maximum normalized value of 900,000 for the Shockley partial. The nickel layer has densities about ten times less than the copper layer for the most active partial dislocations with a maximum normalized value of 50,000 for the Shockley partial.

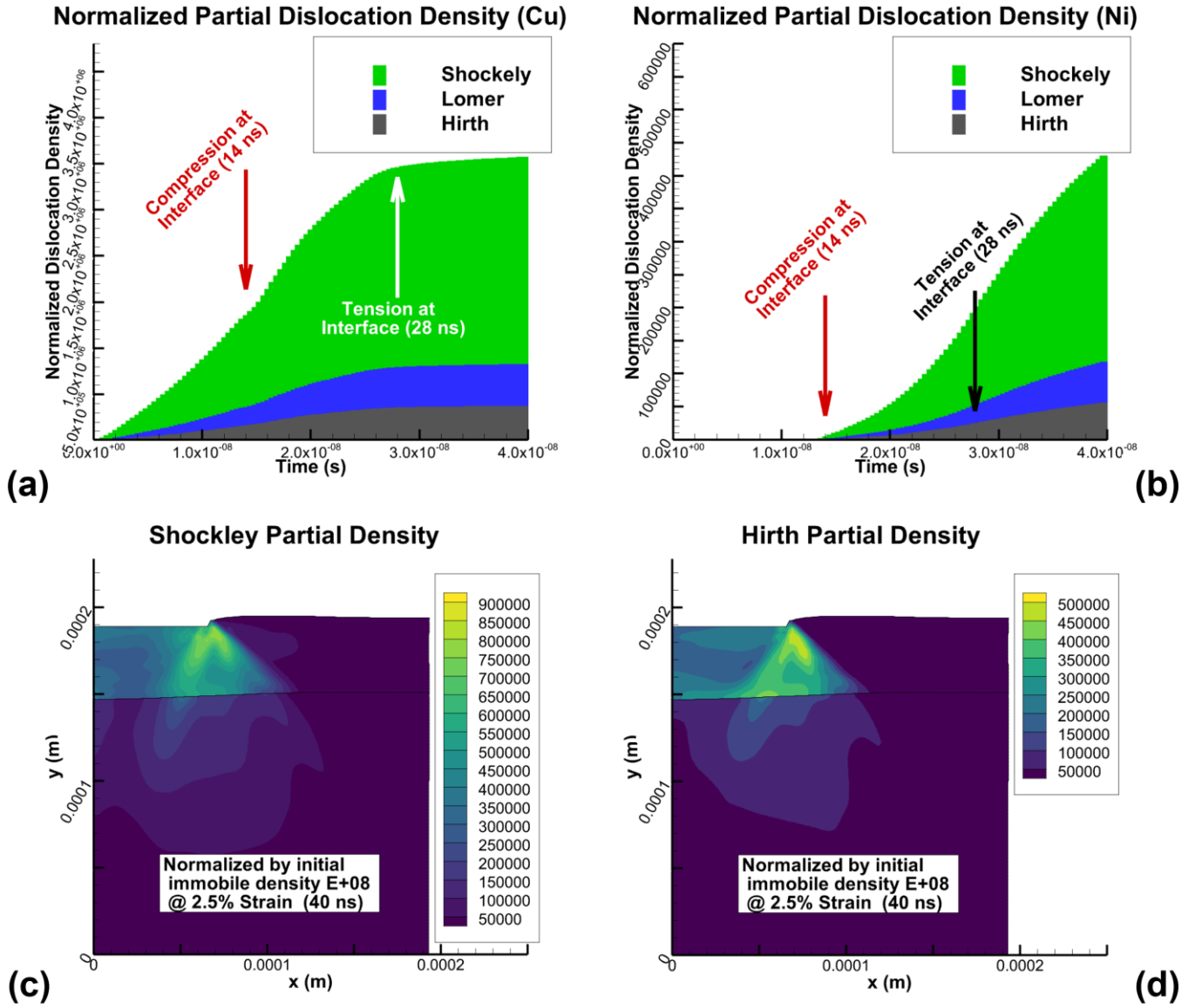

Figure 8. (**a**) Stacking bar charts of normalized partial dislocation densities for the copper layer, and (**b**) for the nickel layer that is activated after the normal stress has reached the interface. (**c**) The density of the dominant Shockley partial dislocation, $\frac{1}{6}[\bar{2}11]$, and (**d**) the dominant Hirth partial dislocation, $^{1}/_{3}[100]$ at a nominal strain of 2.5%.

5. Discussion

Although the scales and modeling approaches are different, the MD and DCP simulations have similar qualitative behavior in several respects. First, both show compressive waves originating from the impactor into the substrate. Second, in both cases, dislocations first form along the impactor edge. For the DCP, these propagate both under and laterally from the impactor, similar to that observed for the higher impact velocity MD simulation. In all cases, these are overwhelmingly Shockley partials. Both methods also exhibit a subsurface tension below the impactor right after the compression waves pass through the interface; however, this effect is much smaller in the MD compared to the DCP simulations. Finally, in the DCP and the higher impact energy MD, the dislocations beneath the impactor reach the interface, and create defects in the nickel. These defects are exclusively Shockley dislocations in the MD, and mostly Shockley in the DCP. Furthermore, in both systems, the number of dislocations in the nickel is significantly less than in the copper, and the dislocation distribution is discontinuous across the buried interface.

Some differences were also observed between the simulations. The primary difference was the formation of interfacial perfect dislocations that spontaneously formed at the copper–nickel interface in the MD. Absent in DCP, these evolved into partial dislocations that expanded into stair-rod and Shockley partials. Another major difference is that the MD simulations needed a larger initial kinetic energy of the impactor to see damage to the same extent as the DCP simulation. This may be due to the difference in how the impactors slowed, and the total amount of energy that is transferred into the substrate.

6. Summary

The impact of a substrate containing a buried copper–nickel interface was investigated using atomistic MD and microstructurally-based DCP simulations, with the goal being to compare and contrast how these methods could be used together across different time and length scales to study a complex micro-mechanical problem. Both methods showed similar qualitative behavior, such as defects originating along the impactor edges, a dominance of Shockley dislocations, and non-continuous dislocations distributions at the buried interface. Differences were also noted, specifically the formation of perfect dislocations at the interface in the MD simulations that were not present in the DCP model. However, these dislocations did not make a significant difference in the overall interfacial defects induced by the impactor. Overall, this favorable comparison between methods justifies assumptions used in both, such as interactions of dislocation densities resulting in partials in the DCP; and that the nanoscale in MD is representative of macroscopic-scale behavior.

Author Contributions: All four others contributed equally to this investigation. All authors have read and agreed to the published version of the manuscript.

Funding: L. Granger and D. Brenner acknowledge funding from the US Department of Defense, Multidisciplinary University Research Initiative through the Army Research Office, Grant # W911NF-16-1-0406. M Chen and M. Zikry acknowledge support from DOE/Los Alamos Grant # 2021-1756/628147.

Institutional Review Board Statement: Not applicable.

Informed Consent Statement: Not applicable.

Data Availability Statement: All data are available upon request.

Conflicts of Interest: The authors declare no conflict of interest.

References

1. Jin, H.; Sanborn, B.; Lu, W.-Y.; Song, B. Mechanical Characterization of 304L-VAR Stainless Steel in Tension with a Full Coverage of Low, Intermediate, and High Strain Rates. *Mech. Mater.* **2021**, *152*, 103654. [CrossRef]
2. Lu, S.; Li, D.; Brenner, D.W. Molecular Dynamics Simulations of Plastic Damage in Metals. In *Handbook of Damage Mechanics*; Voyiadjis, G.Z., Ed.; Springer New York: New York, NY, USA, 2015; pp. 453–486, ISBN 978-1-4614-5588-2.
3. Kositski, R.; Mordehai, D. A Dislocation-Based Dynamic Strength Model for Tantalum across a Large Range of Strain Rates. *J. Appl. Phys.* **2021**, *129*, 165108. [CrossRef]
4. Dixit, N.; Xie, K.Y.; Hemker, K.J.; Ramesh, K.T. Microstructural Evolution of Pure Magnesium under High Strain Rate Loading. *Acta Mater.* **2015**, *87*, 56–67. [CrossRef]
5. Nemat-Nasser, S.; Guo, W.-G.; Kihl, D.P. Thermomechanical Response of AL-6XN Stainless Steel over a Wide Range of Strain Rates and Temperatures. *J. Mech. Phys. Solids* **2001**, *49*, 1823–1846. [CrossRef]
6. Bryukhanov, I.A. Atomistic Simulation of the Shock Wave in Copper Single Crystals with Pre-Existing Dislocation Network. *Int. J. Plast.* **2022**, *151*, 103171. [CrossRef]
7. Neogi, A.; Mitra, N. Evolution of Dislocation Mechanisms in Single-Crystal Cu under Shock Loading in Different Directions. *Model. Simul. Mater. Sci. Eng.* **2017**, *25*, 025013. [CrossRef]
8. Li, C.; Yang, K.; Tang, X.C.; Lu, L.; Luo, S.N. Spall Strength of a Mild Carbon Steel: Effects of Tensile Stress History and Shock-Induced Microstructure. *Mater. Sci. Eng. A* **2019**, *754*, 461–469. [CrossRef]
9. Wang, X.-X.; He, A.-M.; Zhou, T.-T.; Wang, P. Spall Damage in Single Crystal Tin under Shock Wave Loading: A Molecular Dynamics Simulation. *Mech. Mater.* **2021**, *160*, 103991. [CrossRef]
10. Chen, J.; Mathaudhu, S.N.; Thadhani, N.; Dongare, A.M. Correlations between Dislocation Density Evolution and Spall Strengths of Cu/Ta Multilayered Systems at the Atomic Scales: The Role of Spacing of KS Interfaces. *Materialia* **2019**, *5*, 100192. [CrossRef]

11. Dongare, A.M.; Rajendran, A.M.; LaMattina, B.; Zikry, M.A.; Brenner, D.W. Atomic Scale Simulations of Ductile Failure Micromechanisms in Nanocrystalline Cu at High Strain Rates. *Phys. Rev. B* **2009**, *80*, 104108. [CrossRef]
12. Dongare, A.M.; Rajendran, A.M.; LaMattina, B.; Zikry, M.A.; Brenner, D.W. Atomic Scale Studies of Spall Behavior in Nanocrystalline Cu. *J. Appl. Phys.* **2010**, *108*, 113518. [CrossRef]
13. Rice, B.; Sewell, T.; Brenner, D.; Holian, B. Overview of Atomistic Molecular Simulation Methods. In *ITRI Study of Molecular Dynamics Simulations of Detonation Phenomena*; ITRI Press: Laurel, MD, USA, 2003.
14. Hoover, W.G. *Molecular Dynamics*; Lecture notes in Physics; Springer: Berlin/Heidelberg, Germany, 1986; ISBN 978-3-540-16789-1.
15. Shanthraj, P.; Zikry, M.A. Dislocation Density Evolution and Interactions in Crystalline Materials. *Acta Mater.* **2011**, *59*, 7695–7702. [CrossRef]
16. Brenner, D.W.; Robertson, D.H.; Elert, M.L.; White, C.T. Detonations at Nanometer Resolution Using Molecular Dynamics. *Phys. Rev. Lett.* **1993**, *70*, 2174–2177. [CrossRef] [PubMed]
17. Hu, Y.; Brenner, D.W.; Shi, Y. Detonation Initiation from Spontaneous Hotspots Formed During Cook-Off Observed in Molecular Dynamics Simulations. *J. Phys. Chem. C* **2011**, *115*, 2416–2422. [CrossRef]
18. Brenner, D.W.; Shenderova, O.A.; Areshkin, D.A. Quantum-Based Analytic Interatomic Forces and Materials Simulation. In *Reviews in Computational Chemistry*; Lipkowitz, K.B., Boyd, D.B., Eds.; John Wiley & Sons, Inc.: Hoboken, NJ, USA, 2007; pp. 207–239, ISBN 978-0-470-12589-2.
19. Sinnott, S.B.; Brenner, D.W. Three Decades of Many-Body Potentials in Materials Research. *MRS Bull.* **2012**, *37*, 469–473. [CrossRef]
20. Shi, Y.; Brenner, D.W. Simulated Thermal Decomposition and Detonation of Nitrogen Cubane by Molecular Dynamics. *J. Chem. Phys.* **2007**, *127*, 134503. [CrossRef]
21. Shi, Y.; Brenner, D.W. Molecular Simulation of the Influence of Interface Faceting on the Shock Sensitivity of a Model Plastic Bonded Explosive. *J. Phys. Chem. B* **2008**, *112*, 14898–14904. [CrossRef]
22. Daw, M.S.; Baskes, M.I. Embedded-Atom Method: Derivation and Application to Impurities, Surfaces, and Other Defects in Metals. *Phys. Rev. B* **1984**, *29*, 6443–6453. [CrossRef]
23. Holian, B.L. Atomistic Computer Simulations of Shock Waves. *Shock Waves* **1995**, *5*, 149–157. [CrossRef]
24. Germann, T.C.; Holian, B.L.; Lomdahl, P.S.; Ravelo, R. Orientation Dependence in Molecular Dynamics Simulations of Shocked Single Crystals. *Phys. Rev. Lett.* **2000**, *84*, 5351–5354. [CrossRef]
25. Meng, Z.; Keten, S. Unraveling the Effect of Material Properties and Geometrical Factors on Ballistic Penetration Energy of Nanoscale Thin Films. *J. Appl. Mech.* **2018**, *85*, 121004. [CrossRef]
26. Dewapriya, M.A.N.; Miller, R.E. Molecular Dynamics Study of the Mechanical Behaviour of Ultrathin Polymer–Metal Multilayers under Extreme Dynamic Conditions. *Comput. Mater. Sci.* **2020**, *184*, 109951. [CrossRef]
27. Zhang, C.; Kalia, R.K.; Nakano, A.; Vashishta, P.; Branicio, P.S. Deformation Mechanisms and Damage in α-Alumina under Hypervelocity Impact Loading. *J. Appl. Phys.* **2008**, *103*, 083508. [CrossRef]
28. Kolar, H.R.; Spence, J.C.H.; Alexander, H. Observation of Moving Dislocation Kinks and Unpinning. *Phys. Rev. Lett.* **1996**, *77*, 4031–4034. [CrossRef] [PubMed]
29. Voisin, T.; Grapes, M.D.; Li, T.T.; Santala, M.K.; Zhang, Y.; Ligda, J.P.; Lorenzo, N.J.; Schuster, B.E.; Campbell, G.H.; Weihs, T.P. In Situ TEM Observations of High-Strain-Rate Deformation and Fracture in Pure Copper. *Mater. Today* **2020**, *33*, 10–16. [CrossRef]
30. Yan, Z.; Lin, Y. Lomer-Cottrell Locks with Multiple Stair-Rod Dislocations in a Nanostructured Al Alloy Processed by Severe Plastic Deformation. *Mater. Sci. Eng. A* **2019**, *747*, 177–184. [CrossRef]
31. Ledbetter, H.M.; Reed, R.P. Elastic Properties of Metals and Alloys, I. Iron, Nickel, and Iron-Nickel Alloys. *J. Phys. Chem. Ref. Data* **1973**, *2*, 531–618. [CrossRef]
32. Thompson, A.P.; Aktulga, H.M.; Berger, R.; Bolintineanu, D.S.; Brown, W.M.; Crozier, P.S.; in't Veld, P.J.; Kohlmeyer, A.; Moore, S.G.; Nguyen, T.D.; et al. LAMMPS—A Flexible Simulation Tool for Particle-Based Materials Modeling at the Atomic, Meso, and Continuum Scales. *Comput. Phys. Commun.* **2022**, *271*, 108171. [CrossRef]
33. Fischer, F.; Schmitz, G.; Eich, S.M. A Systematic Study of Grain Boundary Segregation and Grain Boundary Formation Energy Using a New Copper–Nickel Embedded-Atom Potential. *Acta Mater.* **2019**, *176*, 220–231. [CrossRef]
34. Ackland, G.J.; Jones, A.P. Applications of Local Crystal Structure Measures in Experiment and Simulation. *Phys. Rev. B* **2006**, *73*, 054104. [CrossRef]
35. Thompson, A.P.; Plimpton, S.J.; Mattson, W. General Formulation of Pressure and Stress Tensor for Arbitrary Many-Body Interaction Potentials under Periodic Boundary Conditions. *J. Chem. Phys.* **2009**, *131*, 154107. [CrossRef] [PubMed]
36. Honeycutt, J.D.; Andersen, H.C. Molecular Dynamics Study of Melting and Freezing of Small Lennard-Jones Clusters. *J. Phys. Chem.* **1987**, *91*, 4950–4963. [CrossRef]
37. Faken, D.; Jónsson, H. Systematic Analysis of Local Atomic Structure Combined with 3D Computer Graphics. *Comput. Mater. Sci.* **1994**, *2*, 279–286. [CrossRef]
38. Stukowski, A.; Bulatov, V.V.; Arsenlis, A. Automated Identification and Indexing of Dislocations in Crystal Interfaces. *Model. Simul. Mater. Sci. Eng.* **2012**, *20*, 085007. [CrossRef]
39. Stukowski, A. Visualization and Analysis of Atomistic Simulation Data with OVITO–the Open Visualization Tool. *Model. Simul. Mater. Sci. Eng.* **2010**, *18*, 015012. [CrossRef]

40. Zikry, M.A. An Accurate and Stable Algorithm for High Strain-Rate Finite Strain Plasticity. *Comput. Struct.* **1994**, *50*, 337–350. [CrossRef]
41. Agarwal, G.; Valisetty, R.R.; Namburu, R.R.; Rajendran, A.M.; Dongare, A.M. The Quasi-Coarse-Grained Dynamics Method to Unravel the Mesoscale Evolution of Defects/Damage during Shock Loading and Spall Failure of Polycrystalline Al Microstructures. *Sci. Rep.* **2017**, *7*, 12376. [CrossRef]